RSC Advances

ROYAL SOCIETY OF CHEMISTRY

www.rsc.org/advances

Cite this: DOI: 10.1039/c0xx00000x

www.rsc.org/xxxxxx

ARTICLE TYPE

Biocompatible Folate-modified Gd^{3+}/Yb^{3+}-doped ZnO Nanoparticles for Dualmodal MRI/CT Imaging

Qi Yin,[a] Xiaoying Jin[a,b] Guocheng Yang,[a,b] Chunhuan Jiang,[c] Zhongkai Song,[a] and Guoying Sun[a,b]*

Received (in XXX, XXX) Xth XXXXXXXXX 20XX, Accepted Xth XXXXXXXXX 20XX

DOI: 10.1039/b000000x

The development of multimodal imaging probes is highly desirable for clinical diagnosis and therapy because they combine the advantages of different imaging functionalities within a single nanoplatform and can provide complementary information from each imaging modality. Herein, we demonstrated our effects to the fabrication of ZnO:Gd,Yb probe for MRI/CT imaging on the basis of the paramagnetic property of Gd^{3+} and the high X-ray absorption property of Yb^{3+}. To increase the stability and biocompatibility, these nanoprobes were functionalized with folate (FA). The cytotoxicity and histological analysis show these nanoparticals (NPs) present low cytotoxicity even at a Gd^{3+} concentration as high as 30 μg mL^{-1} and have no obvious injury or inflammation in the susceptible organs (heart, liver, spleen, lung and kidney). Upon intravenously injected, the uptake and deposition of FA-modified nanoprobes take place primarily in spleen, lung and liver, and but these NPs can be completely excreted out from the body of mice as time prolonged. These nanoprobes not only exhibit a relatively higher longitudinal relaxivity (r_1) of 6.29 mM^{-1} s^{-1} over the commercial Gd(III)-diethylenetriamine pentaacetic acid complexes, but also keep strong X-ray attenuation property. In T_1-weighted magnetic resonance imaging (MRI) and X-ray computed tomography (CT) studies, they can efficiently induce positive contrast enhancement, demonstrating the potential of the as-prepared ZnO:Gd,Yb-FA NPs for the development of dualmodal MRI/CT molecular imaging probes.

INSTRUCTIONS

Chemical imaging probes can play a vital role in clinical diagnosis and therapy, as well as the basic biological research at molecular level.[1,2] With the rapid development of multimode imaging techniques and nanotechnology, multifunctional nanoprobes have been devised to offer more comprehensive diagnostic information and the dynamics of disease progression, because different imaging functionalities can be integrated into a single nanoplatform.[3-8] In addition, nanoprobes can produce high contrast images even at a reduced dose due to a dense population of probing elements, which will in turn lower any danger coming from the toxicity of nanoprobes in the body.

Among various multimodal imaging probes, MRI/optical imaging nanoprobes, mainly based on MRI contrast agents, fluorescent dye and fluorescent quantum dots (QDs) etc, have been one of the rapidly evolving material systems. The major concern associated with these nanoprobes is the limited tissue penetration depth and the lower spatial resolution of fluorescence, which limited their further applications *in vivo*.[9-13] In contrast, MRI/CT dual modal imaging nanoprobes have promising potential because both CT and MRI are essential medical imaging modalities and there is significant clinical complementation between them. MRI can provide unsurpassed 3D soft tissue detail and bone marrow information, while CT is well-known for its high resolution and three dimensional visual reconstruction of tissues of interest.[14-16] Therefore, a large number of MRI/CT imaging nanoprobes have been developed, thereby leading to more precise diagnosis.

Up to now, various strategies have been demonstrated to achieve MRI/CT imaging nanoprobes. One logical strategy was the combination of gadolinium chelates (Gd-DTPA or Gd-DO3A with high relaxation efficiency) with Au nanostructures (nanoparticles, nanorods, as well as nanoclusters with higher atomic number and strong X-ray attenuation property).[17-20] Moreover, Gd-DTPA modified lanthanide-based upconversion nanoparticles were also designed and prepared for MR and CT imaging.[21,22] The other strategy involved the doping of different lanthanide ions into a nanoplatform to achieve multi modal MRI/CT imaging probes.[23] Some research groups are interested in Gd^{3+}-based NPs such as $NaGdF_4$ and Gd_2O_3 as contrast enhancing agents for MRI/CT imaging.[3,24,25] For example, Zhao et al. presented the example of doping Yb^{3+}/Er^{3+} into the nanoplatform of $NaGdF_4$ as trimodal contrast agents for CT/MR/up-conversion luminescence (UCL) image. These uniformly sized NPs possesses excellent biocompatibility and shows good safety, however, these are commonly synthesized by

a sequence of reactions involving high temperature (300 °C) under an argon (Ar) atmosphere in an organic medium.[3] Qu and colleagues reported PEGylated hybrid ytterbia nanoparticles (PEG-Yb_2O_3:Gd) with an average diameter of 120 nm as high-performance diagnostic probes for magnetic resonance and X-ray computed tomography imaging.[23] These nanoprobes exhibited the similar r_1 relaxivity to that of commercially available Magnevist due to the diameter dependence of r_1. Therefore, the design of a simple and efficient strategy for the preparation of multimodal imaging probes with small size are highly desirable because the huge surface to volume ratio (S/V) of the small NPs will couple with the cooperative induction of surface Gd(III) ions to increase the longitudinal relaxation of a water proton.[26] Furthermore, the investigations of their imaging performance, toxicity, as well as biodistribution behavior are also indispensable.

Zinc oxide (ZnO) NPs are well recognized as versatile biocompatible multifunctional materials due to their superior chemical stability under physiological environment, low-toxicity, and adequate dispersibility, etc.[27,28] Hence, ZnO nanomaterials could be one of the excellent candidates as host materials for the construction of novel multi modal nanoprobes. Recently, Lu et al. presented the first example of Gd^{3+}-doped ZnO quantum dots (QDs) as dual modal fluorescence and MRI nanoprobes.[29] Their study demonstrated that such nanoprobes have low toxicity and exert strong positive contrast effect for MRI *in vitro*. Besides, the surface modification methods of these nanoparticles are similar to those of the well developed oxide nanoparticles commonly through silane-based chemical bond formation on metal oxide surfaces. Thus, the surface chemistry could be easily tuned for biological stealth and targeting functions.

Herein, Gd^{3+},Yb^{3+}-doped ZnO nanoparticles (ZnO:Gd,Yb NPs) were fabricated on the basis of the paramagnetic property of Gd^{3+} and the high X-ray absorption of Yb^{3+} (X-ray absorption coefficient of 6.91 cm^2 g^{-1} at 80 keV)[30,31] and explored for the potentials as a dualmodal MRI /CT imaging probe (Scheme 1). We used a facile homogeneous precipitation method to prepare these NPs at relative low temperature and modified their surface with biocompatible folate. The stability, relaxivity and X-ray attenuation properties of these nanoparticles were firstly investigated in detail. Then, the toxicity and biodistribution of ZnO:Gd,Yb-FA NPs were systematically assessed, which indicated that our uniformly sized nanoprobes possessed excellent biocompatibility and could be excreted out from the body gradually. Importantly, this work demonstrated that our well-prepared ZnO:Gd,Yb-FA NPs could obviously brighten the signal of the MRI and X-ray CT imaging *in vitro* and had great potential in biological and medical fields in the future.

EXPERIMENTAL SECTION

Materials

Zinc acetate dihydrate was purchased from Tianjin Fuchen chemical reagents factory (Tianjin, China). Gadolinium acetate hydrate, ytterbium acetate tetrahydrate, folate, N-hydroxysuccinimide (NHS) and N,N'-dicyclohexylcarbodiimide (DCC) were procured from Sigma-Aldrich. 3-(2-aminoethylamino)propyltriethoxysilane (AEAPS) was obtained from Fluorochem Ltd (UK). Tetramethylammonium hydroxide (TMAH) was purchased from J&K chemical Ltd. The water was deionized by Millipore Milli-Q purification system.

Synthesis of multifunctional contract agents

Synthesis of folate-NHS

Folate (0.227 mmol) and DCC (0.454 mmol) were dissolved in anhydrous dimethyl sulfoxide (DMSO). After magnetic stirring for 15 min, NHS (0.182 mmol) was added into the mixture. The reaction was allowed to proceed for 6 h at room temperature. The reaction mixture was centrifuged at 10000 rpm for 30 min to remove the precipitates. The obtained supernatant was quickly transferred with cold anhydrous diethyl ether and acetone (7:3, v/v) to produce yellow precipitates. After washing with the above cold solution for several times, the folate-NHS was collected by centrifugation and dried under the vacuum condition.

Synthesis of ZnO:Gd,Yb nanoparticles

ZnO:Gd,Yb nanoparticles were synthesized by the method of homogeneous precipitation. In a typical approach, $Zn(CH_3COO)_2{\cdot}2H_2O$ (1.2 mM, 0.2634 g), $Gd(CH_3COO)_3{\cdot}xH_2O$ and $Yb(CH_3COO)_3{\cdot}4H_2O$ were codissolved into 20 mL of absolute ethanol in a round-bottomed flask. Oleic acid (70 μL) was added to the solution, and then the mixture was heated to reflux under constant stirring. TMAH (0.526 mL) in 5 mL of refluxing ethanol was rapidly transferred into this mixture under vigorous stirring. After stirring for 3 min, 50 mL of ethanol was added and putted immediately in an ice bath for cooling. The resulted oleate-stabilized ZnO:Gd,Yb was obtained by centrifugation and washed with ethanol under ultrasonic treatment for three times, and finally redispersed in 10 mL of toluene for the subsequent experiments. The molar ratios of gadolinium acetate hydrate, ytterbium acetate hydrate with zinc acetate dihydrate were 0, 0.03, 0.08, 0.1, 0.2 and 0.3 in different experiments, which were designed as x.

Preparation of ZnO:Gd,Yb-NH_2 NPs

AEAPS (25 μL) dispersed in 1 mL toluene was added to the above solution under ceaseless stirring at room temperature. After 5 min, TMAH pentahydrate (0.0182 g) in 1 mL ethanol was injected. The reactants were refluxed at 85 ºC for 45 min and then cooled down to room temperature. As-prepared ZnO:Gd,Yb-NH_2 NPs were gained by repeating the procedures of centrifugation and washing with toluene for several times.

Surface modification of ZnO:Gd,Yb-NH_2 NPs

Folate-NHS, ZnO:Gd,Yb-NH_2 and TEA (triethylamine) were codissolved in anhydrous DMSO under vigorous stirring at room temperature. After stirring for 48 h while avoiding light, the resulting solid was centrifuged at 9000 rpm for 30 min. The final samples were washed with DMSO and deionized water respectively for three times to ensure the removal of unreacted reactants.

Characterization and instruments

Powder X-ray diffraction (XRD) studies were conducted on a D/Max-IIB diffractometer at a scanning rate of 4° min^{-1}, in the 2θ range of 20-80°. The workup procedure was carried out with Cu Kα1 radiation (λ = 1.5406 nm). Fourier transform infrared (FT-IR) spectra were collected on a Fourier Transform Infrared

Spectrophotometer Magna 560 by using KBr pellets. UV-vis experiments were carried out with Cary50 ultraviolet spectrophotometer (Varian USA). High resolution transmission electron microscope (HRTEM) images were taken with a JEOL-2100F electron microscope operated at 200.00 kV accelerating voltage. The sample was prepared in absolute ethyl alcohol. X-ray photoelectron spectrometry (XPS) spectra were taken with a VG ESCALAB MKII spectrometer using a microfocused, manochromatic Al Kα. Inductively coupled plasma-optical emission spectrometer (ICP-OES, PerkinElmer) was utilized to analyze the Gd element content of the products dispersed in ultrapure water. The 1H NMR spectra and relaxation times of the samples were carried out at 30 ºC with 9.4 T Bruker avance III 400 MHz nuclear magnetic resonance spectrometer (Germany).

Toxic effects of ZnO:Gd,Yb-FA.

In vitro cytotoxicity was assessed by implementing methyl thiazolyl tetrazolium (MTT) assays on the HeLa cells. Cells were seeded at the culture medium using 37 ºC in an atmosphere of 95% air and 5% CO_2 for 24 h. Different concentrations of the as-prepared ZnO:Gd,Yb-FA (x = 0.1) were then added to the culture medium for another 24 h. Whereafter, MTT (100 ml, 10%) reagent was introduced and incubated for an additional 4 h in order to form purple formazan dye. The assay plate was then allowed to dissolve in DMSO for 15 min. Finally, the optical absorbance of the colored solution was quantified measured at 570 nm certain wavelength by an enzyme-linked immunosorbent assay reader. The following formula was used to calculate the inhibition of cell growth:

Cell viability (%) = (mean of Abs. value of treatment group/mean of Abs. value of control) × 100%.

For *in vivo* toxicity, the histological assessment was further investigated by injecting ZnO:Gd,Yb-FA NPs (0.16 mg Gd/kg) into the wistar mice through tail vein injection (n = 3), which were the test group. Wistar mice (n = 3) without injection were selected as the control group. The heart, liver, spleen, lung, kidney, muscle and blood were removed from the mice after 7 days, and fixed in formaldehyde, embedded in paraffin, sectioned, and stained with hematoxylin and eosin.

Biodistribution.

Experimental animals were Wistar male mice (~150 g). All the animal experiments were done in compliance with the national laws governing control and supervision of experiments on animals. For biodistribution, ZnO:Gd,Yb-FA NPs were used to inject to the mice via the tail vein. Determination of Gd element content in the organs (heart, liver, spleen, lung, kidney, muscle, blood) was performed by ICP-OES analysis at 1-h, 2-d, 7-d, 15-d and 30-d post-injection. A total of 15 mice were employed to yield the average values of 3 mice at each time points. The percentage of added dose per gram (% ID/g) for each organ was calculated by comparing Gd element content, the values expressed as mean ± standard deviation (SD) for each time point.

In vitro T_1 MRI and CT imaging.

For *in vitro* T_1-weighted MRI, a series of various concentrations of ZnO:Gd,Yb-FA NPs (Gd mg mL^{-1} = 0, 0.05, 0.1, 0.2, and 0.4 mg mL^{-1}) were prepared in a suite of 1.5 mL tubes for phantom test by using a 1.5 T MRI instrument (SIEMENS MAGNETOM Avanto). As well *in vitro* CT image, various concentrations of ZnO:Gd,Yb-FA NPs (Yb mg mL^{-1} = 0, 1.0, 2.5, 4.0 and 5.0 mg mL^{-1}) and appropriate concentration iohexol were prepared severally in a suite of 1.5 mL tubes. CT images were acquired using Philips Brilliance iCT type 256 scanners. Hounsfield units (HU) values were measured by Brilliance Workspace 4.0 (Philips Healthcare).

RESULTS AND DISCUSSION

Synthesis and characterization

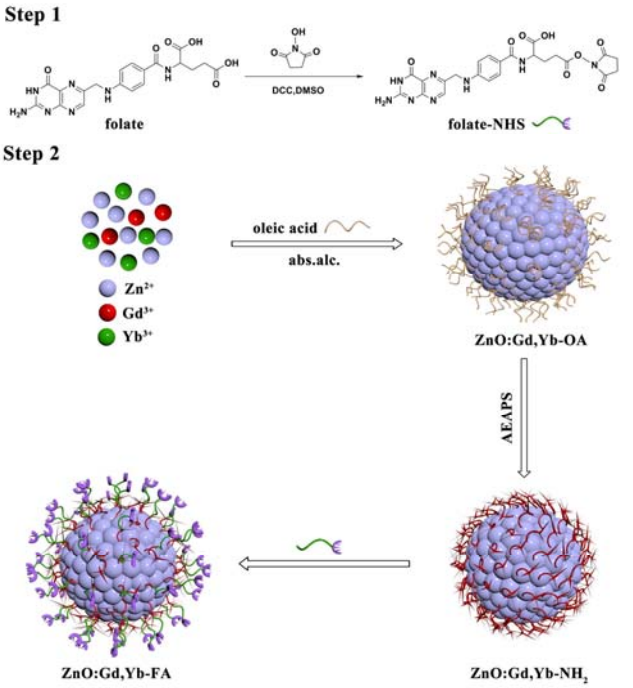

Scheme 1. Schematic illustration of the synthesis of folate-NHS (Step 1), and the preparetion and surface modification of ZnO:Gd,Yb NPs (Step 2).

The schematic representation for the preparation and modification of ZnO:Gd,Yb NPs is shown in Scheme 1. NHS ester of folate was firstly synthesized through a classical condensation reaction of folate and N-hydroxysuccinimide (step 1), which was identified by ^{1}H NMR spectroscopy (Figure S1). OA-stabilized ZnO:Gd,Yb NPs were then prepared by hydrolyzing zinc acetate, gadolinium acetate and ytterbium acetate in absolute ethyl alcohol at 80 ºC. The as-prepared nanoparticles were hydrophobic, which hindered their utility in the biological field. To render them hydrophilic, amine functionalization of ZnO:Gd,Yb NPs were achieved by hydrolyzing AEAPS to form silane-oxygen chemical bond on the surface of NPs. Finally, the amine modified ZnO:Gd,Yb NPs reacted with NHS ester of folate to obtain folate-decorated ZnO:Gd,Yb (ZnO:Gd,Yb-FA) NPs. Folate has high affinity to the folate binding proteins (FBPs), which are overexpressed in many malignant tissue cell membranes.[32-34] The hydrophilic ZnO:Yb,Gd-FA nanoprobes were ready for *in vivo* biodistribution and bioimaging investigation. The actual molar ratios of Gd,Yb/Zn in the final products were ascertained by ICP-OES (Table S1). It is worthy to note that the actual Yb content in ZnO

nanoparticles is much higher than that of Gd, although the nominal contents are equal. The key to any chemical precipitation is the degree of supersaturation, S, given by

$$S = a_A a_B / K_{sp}$$

where a_A and a_B are the activities of the partially hydrolyzed cation ($[Ln(OH)_x(H_2O)_y]^{3-x}$, $x + y = 6$, Ln = Gd, Yb) and anion, respectively, and K_{sp} is the solubility product constant. Nucleation starts only when S reaches the critical supersaturation S*. The lanthanide contraction phenomena reveal a lower solubility (smaller K_{sp}) of $Yb(OH)_3$ than that of $Gd(OH)_3$ in water, from which it can be deduced that the S value is larger for $Yb(OH)_3$ and hence stable nuclei of $Yb(OH)_3$ are relatively easy to form.[35] Therefore, it is not surprising that the actual Yb content in ZnO nanoparticles is much higher than that of Gd. In a control experiment, doping-free ZnO NPs were prepared through the similar preparation process.

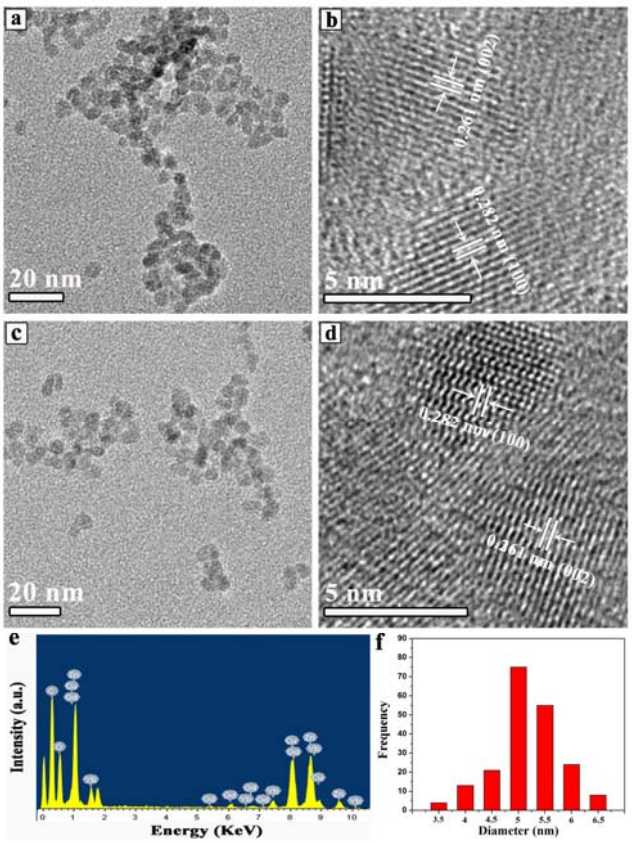

Figure 1. TEM and HRTEM images of ZnO-OA (a and b) and ZnO:Gd,Yb-FA with the x value of 0.1 (c and d), respectively. X-ray energy dispersive spectroscopy (EDS) of ZnO:Gd,Yb-FA (e). Histogram of the particle size distribution of ZnO-OA (f).

Typical TEM images of ZnO-OA and ZnO:Gd,Yb-FA are shown in Figure 1a, c, respectively. The OA-stabilized ZnO NPs are uniform spheres in morphology with diameter ranging from 4 nm to 6 nm. Their average diameter is calculated to be approximately 5.34 ± 0.70 nm via counting two hundred NPs from TEM images (Figure 1f). After doped with rare earth and decorated with folate, the prepared ZnO:Gd,Yb-FA NPs remain the roughly same size and shape as those of ZnO-OA (Figure 1c). The TEM images confirm that the particle sizes decreases with the increase of x value (Figure S2). Notably, spherical shape is generally considered as the proper, biocompatible geometry for bio-applications.[36] The high-resolution TEM (HRTEM) images of ZnO-OA and ZnO:Gd,Yb-FA exhibit well-defined lattice fringe spacing of ca 0.282 nm and 0.261 nm, corresponding well to the (100) and (002) planes of wurtzite structure ZnO crystal, respectively. The presences of Gd, Yb, C and O in the as-prepared samples were confirmed by X-ray energy dispersive spectroscopy (EDS) (Figure 1e). However, N element did not be detected probably due to the close atomic number to C and O or the relatively low content in the product.

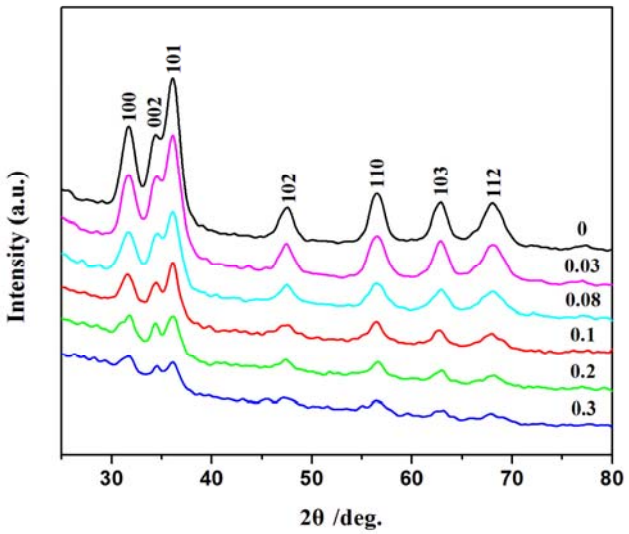

Figure 2. XRD patterns of ZnO-OA and ZnO:Gd,Yb-FA NPs with different x values.

X-ray diffraction (XRD) measurements were carried out to determine the crystallinity of ZnO-OA and ZnO:Gd,Yb-FA NPs (Figure 2). The diffraction peaks of all achieved samples in the XRD patterns can be unambiguously indexed and assigned to the typical wurtzite structure ZnO phase, with a hexagonal crystal system (space group P63mc, a = b = 3.25010 Å, c = 5.20710 Å, $\alpha = \beta = 90°$ and $\gamma = 120°$; JCPDS card no. 01-079-2205)[37]. No any reflection peaks from Yb_2O_3 and Gd_2O_3 can be noticed, which may be due to the formation of amorphous species. The reflection peak intensity becomes weaker apparently as x value increases, indicating the crystallinity of the samples decreases. Furthermore, the average particle size D is estimated according to Debye-Scherer formula:

$$D = K\lambda/(\beta\cos\theta)$$

where K = 0.89, λ (nm) represents the wavelength of Cu Kα1 radiation, θ is the Bragg angle of the X-ray diffraction peak, and β stands for the corrected half width of the diffraction peak. It is found that the particle sizes estimated according to the XRD peaks (110) decreases with the increase of x value (Table S1), consistent with the result of TEM.

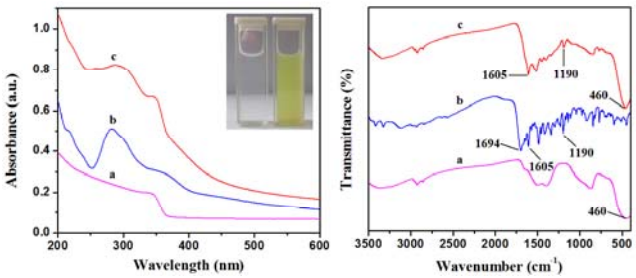

Figure 3. UV-vis spectra (left panel) and FT-IR spectra (right panel) of ZnO:Gd,Yb-NH_2 (a), folate (b) and ZnO:Gd,Yb-FA (c). The inset is the cuvette color photos of ZnO:Gd,Yb-NH_2 (left) and ZnO:Gd,Yb-FA (right), respectively.

The successful surface modification with folate is confirmed by UV-vis and Fourier-transform infrared (FT-IR) spectra (Figure 3). The UV-vis absorption spectrum of ZnO:Gd,Yb-NH_2 NPs exhibits a strong absorption band at about 342 nm corresponding to the electron transitions from the valence band to conduction band (band-to-band transition) of ZnO.[38,39] After decorated with folate, a new peak appears at approximately 283 nm, which corresponds to π-π* transition of pterin ring in folate, suggesting that folate have been successfully engrafted onto the surface of ZnO:Gd,Yb-NH_2 NPs.[40,41] Moreover, the color of NPs dispersions before and after functionalization with folate changed from colourless to yellow (Figure 3), indicating that the ZnO:Gd,Yb-FA NPs have been prepared. To further prove the successful modification of folate, the FT-IR spectra of folate, ZnO:Gd,Yb-NH_2 and ZnO:Gd,Yb-FA nanoprobes are recorded. The peak at 460 cm^{-1} in the curves of ZnO:Gd,Yb-NH_2 and ZnO:Gd,Yb-FA NPs is attributed to the stretching vibration modes of Zn-O.[42] After decorated with folate, the appearance of bands at 1605 cm^{-1} and 1190 cm^{-1} is derived from N-H bending vibration and C-N stretching vibration of folate, respectively.[43,44] Moreover, the disappearance of band at 1694 cm^{-1} is due to the chang of carboxyl groups to amido bonds after amidation reaction.[45]

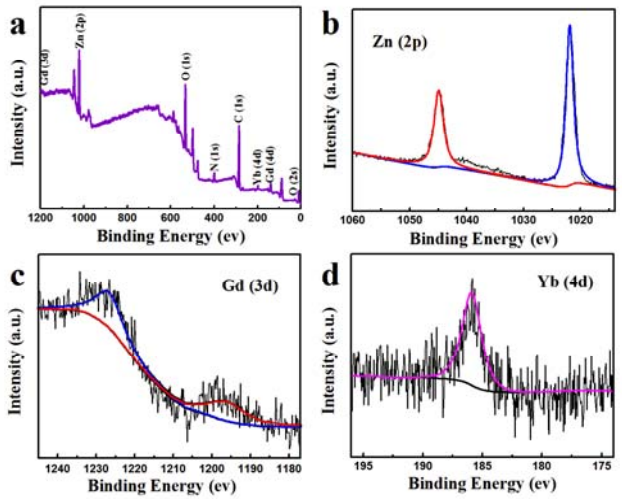

Figure 4. The XPS survey spectrum of prepared ZnO:Gd,Yb-FA NPs (a). High resolution scan corresponding to Zn 2p (b), Gd 3d (c), and Yb 4d (d) region.

XPS is a selective and sensitive surface characterization technique to determine the chemical compositions of materials, and it is also effective in investigating the characteristics (valence) of the constituent atoms (ions) by monitoring their binding energies. The survey spectrum of ZnO:Gd,Yb-FA NPs mainly shows carbon, oxygen, nitrogen, gadolinium, ytterbium and zinc species (Figure 4a). Besides, higher-resolution spectra were also recorded to understand the electronic states of the elements. In the Zn 2p high resolution XPS spectrum, two peaks at 1021.9 eV and 1044.9 eV correspond to the binding energies of Zn $2p_{3/2}$ and Zn $2p_{1/2}$, respectively, which is consistent with the emission of 2p photoelectrons from ZnO.[46] Furthermore, the Gd 3d spectrum consists of a spin orbit split doublet located at about 1227.4 eV for Gd $3d_{3/2}$ and 1197.2 eV for Gd $3d_{5/2}$, respectively. This indicate that the Gd ions in the NPs are of +3 states and exists in the form of Gd_2O_3.[47] The detectable peak of the Yb 4d spectrum centered at 185.9 eV can be attributed to the Yb $4d_{5/2}$, which is in good agreement with the Yb 4d binding energy of Yb_2O_3.[48] Therefore, the above results further demonstrated that the doping of Gd^{3+}, Yb^{3+} ions had successfully been achieved.

Toxicity

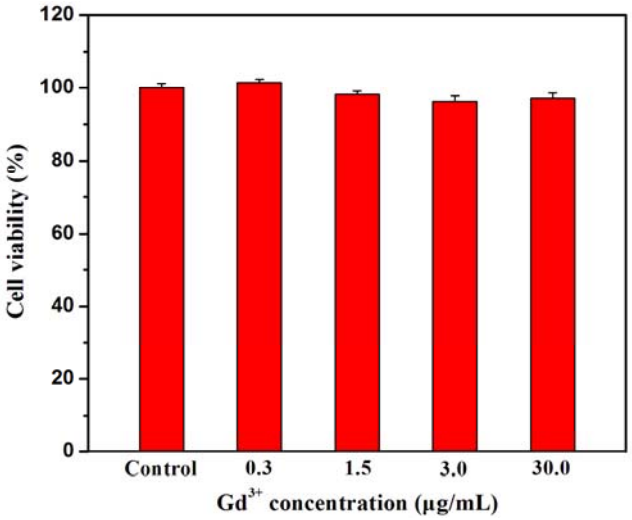

Figure 5. Cell viability estimated by MTT assay after incubated with various concentration of Gd,Yb-doped NPs (x = 0.1) for 24 h.

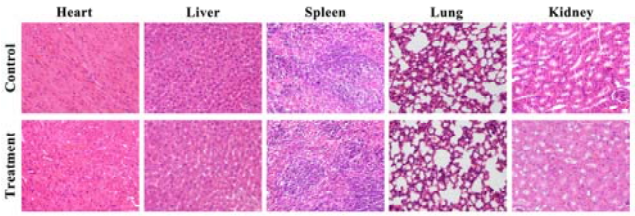

Figure 6. H&E-stained organ sections harvested from mice before and 7 days after injection of ZnO:Gd,Yb-FA NPs. No noticeable abnormality was observed in major organs including heart, liver, spleen, lung, and kidney.

Prior to the application in cell and animal experiments, the stability of the as-prepared ZnO:Gd,Yb-FA NPs was carefully investigated under different physiological conditions, including different pH buffer solution and different concentration salt solution. As shown in Figure S3, the absorbances of the as-prepared NPs are not obviously changed in the buffer solution containing different concentration of NaCl, so are in well-balanced pH = 6.8-7.5. The disintegration of ZnO NPs in mildly acidic medium leads to the slightly decline in absorbances, while the absorbances are slightly increased in weak alkaline environment because of the existence of folate (Figure S4). The results above indicate the NPs have excellent stability in the normal physiological conditions (well-balanced pH value is in a narrow range of 7.35-7.45 and the concentration of saline solution is 0.9%) to be applied into the body. Potential toxic effects have always been the major obstacle for the application of nanomaterials in biomedicine region. Cytotoxicity and histological assessments are the two major methods to the toxic effects. The cytotoxicity of ZnO:Gd,Yb-FA NPs was firstly investigated by MTT assay because it is usually considered as one of the most preliminary parameters for the clinical application of biomaterials. The viability of Hela cells after 24 h exposure to the as-prepared nanoprobes is depicted in Figure 5. Encouragingly, the cell viability and proliferation are not hindered after 24 h incubation with the present of ZnO:Gd,Yb-FA

NPs at the dose of 0.3 μg mL^{-1}. Even at a relatively high concentration of 30 μg mL^{-1}, the cell viability still maintained 97%. These preliminary experimental results indicate the low toxicity of ZnO:Gd,Yb-FA nanoprobes and the potential application for *in vivo* imaging. In comparison with the traditional semiconductor QDs, the Zn-based nanoprobes should hold a great promise in clinical applications due to their much lower toxicity than that of heavy metal-based QDs. Toxicity was further investigated by the histological assessment of the organ (heart, liver, spleen, lung, and kidney) collected from the mice at 7 d after intravenous administration of ZnO:Gd,Yb-FA NPs (0.16 mg Gd/kg). As shown in Figure 9, no obvious injury or any other adverse effect is found in the five susceptible organs and their morphological structures are still normal. The above preliminary experimental results indicate that the toxicity of the ZnO:Gd,Yb-FA NPs is negligible at our tested dose, but further investigation of the chronic toxicity of the NPs is still required before clinical application.

Biodistribution.

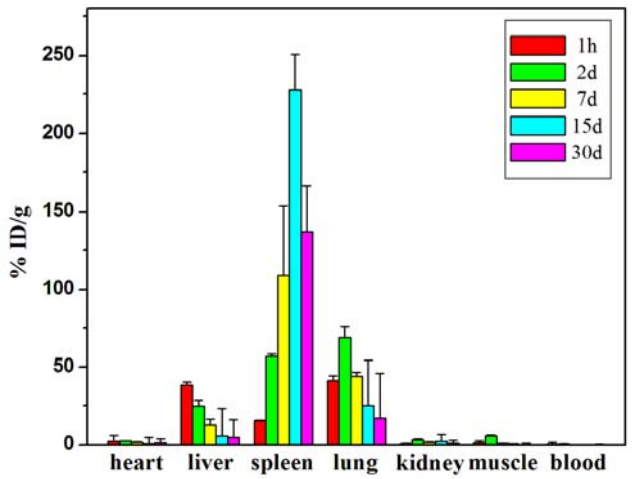

Figure 7. Biodistribution of the prepared ZnO:Gd,Yb-FA NPs (x = 0.1) at 1 h, 48 h, 7 d, 15 d and 30 d post-injection via the tail vein of Wistar mice. Date represent mean ± SD (n = 3).

For the bioapplications *in vivo*, one of the major issues is the fate of these nanoprobes post injection by vein. To preliminary understand the relative biodistribution of ZnO:Gd,Yb-FA NPs, fluorescence imaging *in vitro* of various main organs (heart, liver, spleen, lung, kidney) from the mouse at 1 h post-injection of the doping-free ZnO-FA NPs, which can emit yellow-green fluorescence, have been conducted. As presented in Figure S5, the remarkable yellow-green fluorescence signal can be observed in liver, spleen and lung. No obvious fluorescence signal can be detected from heart and kidney. To quantify the biodistribution of ZnO:Gd,Yb-FA NPs (x = 0.1), elemental Gd levels in various organs and tissues were measured by ICP-OES at various time intervals after intravenous injection. As shown in Figure 7, at 1 h post injection, most nanoparticles accumulated predominantly in liver and spleen through the mononuclear phagocytes in the reticuloendothelial system (RES). Additionally, a much larger uptake in lung sections may be due to the NPs aggregation right after being injected into the blood, leading to the retention in the capillary vessels of lung. In contrast, the distributions in heart, kidney, and muscle are very low at any time post administration. Similarly, the relative low uptake of PEG-EuOF with the diameter of 5 ± 1.5 nm in the heart, kidney and other organs was also observed.[49] After 2 days, the values of % ID/g in liver and lung gradually decrease. While the value for spleen tissue continue to increase and reach the maximum (227.5 ± 23.25% ID/g) after 15 days, which is a much larger uptake versus liver and lung by reason that the spleen is the largest organ of immune system. And then the % ID/g value gradually reduce 30 days after injection, which is associated with the excretion of the ZnO:Gd,Yb-FA NPs. The above results indicate that the injected NPs are able to be completely excreted out from the mice as time prolonged. According to the Gd element content in blood at 0.25, 1, 6, 24, 48 and 96 h post-injection, the blood half time can be obtained that reached to 5.39 h. (Figure S6)

Relaxivity and T_1-weighted MR imaging *in vitro*.

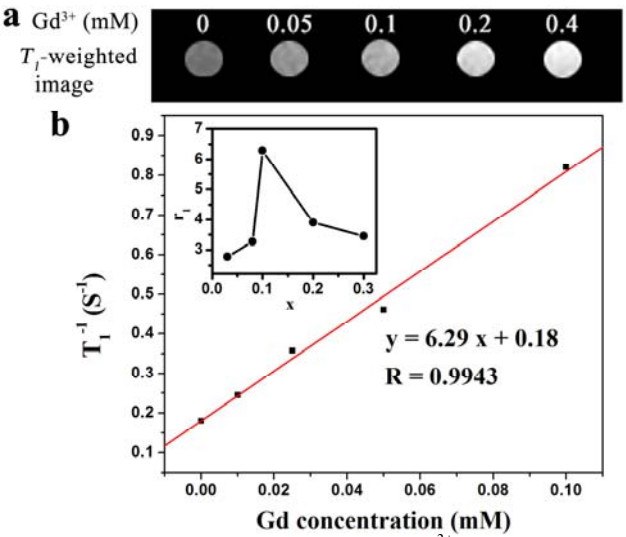

Figure 8. T_1-weighted MRI for various Gd^{3+} concentrations of Gd-doped NPs (x = 0.1) in water at 1.5 T (a). The linear relationship between T_1 relaxation ($1/T_1$) and Gd-doped NPs (b), the inset is the relaxation efficiency of NPs with the change of Gd^{3+} doping amount.

To improve the contrast of MRI, Gd^{3+} complexes have been utilized to efficiently shorten the longitudinal relaxation time (T_1) of water protons due to the large electron spin magnetic moment ($^8S_{7/2}$) and the low spin relaxation of S-state electronic of Gd^{3+}. To evaluate the present NPs as a T_1-weighted MR imaging probe, the phantom images of ZnO:Gd,Yb-FA NPs at different Gd concentrations (0-0.4 mM) was examined at a 1.5 T human clinical scanner. As demonstrated in Figure 8a, a concentration-dependent positive signal enhancement effect can be clearly observed. For further characterization, the T_1 of different concentration NPs suspensions were tested by a standard inversion recovery sequence at 9.4 T. The slope of relaxation rate as a function of Gd^{3+} ion concentrations is the nuclear longitudinal relaxivity (r_1) which determine whether the NPs could be used as the clinical contrast agents and evaluate their MRI contrast efficiency. As shown in Figure 8, the r_1 relaxivity values of ZnO:Gd,Yb-FA NPs increase firstly and reduce afterward with the increase of Gd^{3+} ion doping amount and reach as high as 6.29 mM^{-1} s^{-1} when the x value is 0.1, which is relatively higher than that of the clinicl Gd-DTPA (r_1 = 4.5 mM^{-1} s^{-1}, 1.5 T), the PEG modified $NaYF_4$:Yb^{3+}/Tm^{3+} @ $NaGdF_4$:Yb^{3+} (r_1 = 1.3725 mM^{-1} s^{-1}, 1.5 T)[50] and the folate conjugated $NaGdF_4$:Yb/Er@$NaGdF_4$ (r_1 = 1.64 mM^{-1} s^{-1}, 4.7 T)[3]. In any case, the pronounced signal-enhancement for T_1-weighted images as well as the significantly enhanced r_1 relaxivity demonstrate that

the as-prepared ZnO:Gd,Yb-FA NPs could be employed as an effective contrast probe in MR imaging.

CT imaging *in vitro*.

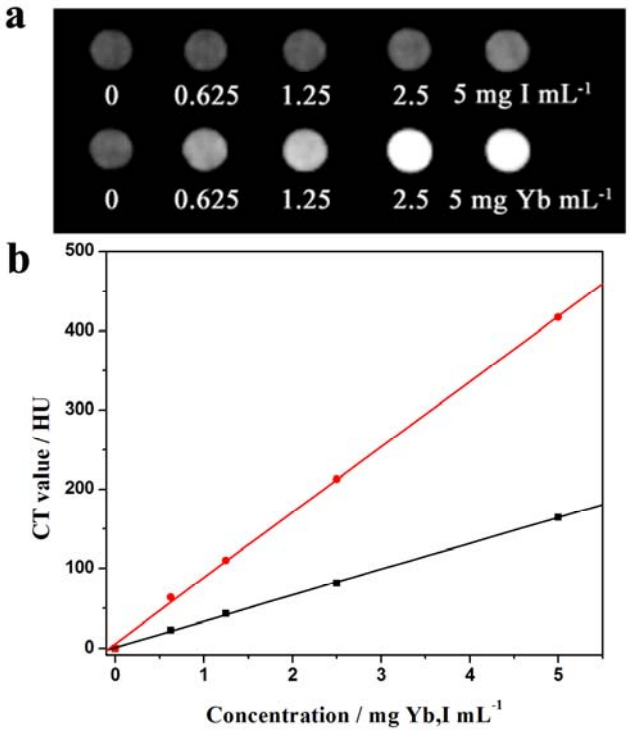

Figure 9. CT images of ZnO:Gd,Yb-FA NPs and iohexol solutions with different concentration of Yb and I (a), respectively. CT value (HU) of ZnO:Gd,Yb-FA NPs (red squares) and iohexol (black circles) as a function of the concentration of Yb (red trace) and I (black trace), respectively (b).

Among the lanthanide ions, Yb has high atomic number (Yb: 70), high X-ray absorption coefficient (Yb: 6.91 cm^2 g^{-1} at 80 keV) , as well as large K-edge energy (Yb k-edge: 61.3 keV). Therefore, Yb-based NPs have been introduced as potential candidates for X-ray CT contrast agents. To assess the CT contrast efficiency, the X-ray attenuation ability of the as-prepared ZnO:Gd,Yb-FA NPs is compared to that of iohexol, the most widely used CT contrast agent in clinic. Figure 9a exhibits the X-ray CT phantom images of ZnO:Gd,Yb-FA NPs and iohexol solutions with different concentration of Yb and I, respectively. As the probe concentration increase, the signal of both CT images measured at 120 kVp obviously brightens. However, the as-prepared NPs produce significantly higher contrast enhancement than the traditional iohexol at equivalent concentrations. To evaluate quantitatively the X-ray attenuation ability of these agents, the linear curve between the HU value and the concentrations of Yb (I) is created by setting the CT value of deionized water as zero. As illustrated in Figure 9b, the CT values increase linearly with the concentration of both contrast agents. Furthermore, the slope of the HU value for ZnO:Gd,Yb-FA NPs is about 82.50 HU L g^{-1}, which is much higher than that of iohexol (32.60 HU L g^{-1}), the PEG modified $NaYF_4$: Yb^{3+}/Tm^{3+} @ $NaGdF_4$: Yb^{3+} (45.83 HU L g^{-1}, 120 kVp)[50] and the PEGylated Gd_2O_3:Yb^{3+}, Er^{3+} (52 HU L g^{-1}, 120 kVp)[25]. These results demonstrate that the as-prepared NPs have better X-ray attenuation property than conventional iodine-based small molecular CT contrast agents under the same concentrations. This good X-ray attenuation performance of ZnO:Gd,Yb-FA NPs is essential for their applications as contrast agents in sensitive CT imaging.

Conclusions

In summary, a dualmodal MRI/CT nanoprobe, ZnO:Gd,Yb-FA NPs with a diameter of 4-6 nm, has been successful designed and prepared via a simple, versatile and environmentally friendly method. The well decoration of folate improves the hydrophily of the NPs which is beneficial for *in vivo* biomedical applications. The toxicity and biodistribution studies indicate that ZnO:Gd,Yb-FA NPs have relatively low cytotoxicity, ignorable potential toxicity *in vivo*, and can be cleared from the bodies of injected mice. Furthermore, the as-prepared NPs are also superior in both MRI and CT imaging *in vitro*. Combining excellent tissue penetration depth of MRI with high-resolution 3D visual reconstruction of CT, these as-prepared ZnO:Gd,Yb-FA NPs are expected to have promising applications in biological, medical and other fields.

Notes and references

[a]*Chemistry and Life Science School, Changchun University of Technology, 2055 Yanan Street, Changchun, P. R. China. Tel: +86-43185716671; E-mail: sunguoying@mail.ccut.edu.cn*
[b]*Advanced Institute of Materials Science, Changchun University of Technology, 2055 Yanan Street, Changchun, P. R. China.*
[c]*State Key Laboratory of Electroanalytical Chemistry, Changchun Institute of Applied Chemistry, Chinese Academy of Sciences, 5625 Renmin Street, Changchun, P. R. China.*

† Electronic Supplementary Information (ESI) available: ^{1}H NMR spectra of folate, NHS and folate-NHS; UV-vis spectra of FA-modified ZnO:Gd,Yb NPs and folate; Fluorescence imaging of several organ. See DOI: 10.1039/b000000x/

1 K. Ding, L. Jing, C. Liu, Y. Hou and M. Gao, *Biomaterials*, 2014, **35**, 1608-1617.
2 W. Xu, K. Kattel, J. Y. Park, Y. Chang, T. J. Kim and G. H. Lee, *Physical chemistry chemical physics : PCCP*, 2012, **14**, 12687-12700.
3 G. Tian, W. Yin, J. Jin, X. Zhang, G. Xing, S. Li, Z. Gu and Y. Zhao, *J. Mater. Chem. B*, 2014, **2**, 1379-1389.
4 G. Tian, Z. Gu, X. Liu, L. Zhou, W. Yin, L. Yan, S. Jin, W. Ren, G. Xing, S. Li and Y. Zhao, *J. Phys. Chem. C*, 2011, **115**, 23790-23796.
5 A. Louie, *Chem. Rev.*, 2010, **110**, 3146-3195.
6 C. Li, T. Chen, I. Ocsoy, G. Zhu, E. Yasun, M. You, C. Wu, J. Zheng, E. Song, C. Z. Huang and W. Tan, *Advanced Functional Materials*, 2014, **24**, 1772-1780.
7 H. Yang, C. Qin, C. Yu, Y. Lu, H. Zhang, F. Xue, D. Wu, Z. Zhou and S. Yang, *Advanced Functional Materials*, 2014, **24**, 1738-1747.
8 J. M. Janjic, P. Shao, S. Zhang, X. Yang, S. K. Patel and M. Bai, *Biomaterials*, 2014, **35**, 4958-4968.
9 E. S. Shibu, K. Ono, S. Sugino, A. Nishioka, A. Yasuda, Y. Shigeri, S.-i. Wakida, M. Sawada and V. Biju, *ACS Nano*, 2013, **7**, 9851-9859.
10 K. Zheng, D. Zhang, D. Zhao, N. Liu, F. Shi and W. Qin, *Physical chemistry chemical physics : PCCP*, 2010, **12**, 7620-7625.
11 X. Hu, M. Wang, F. Miao, J. Ma, H. Shena and N. Jia, *J. Mater. Chem. B*, 2014, **2**, 2265-2275.
12 K. M. Yang, H.-I. Cho, H. J. Choi and Y. Piao, *J. Mater. Chem. B*, 2014, **2**, 3355-3364.
13 A. Abdukayum, C. X. Yang, Q. Zhao, J. T. Chen, L. X. Dong and X. P. Yan, *Analytical chemistry*, 2014, **86**, 4096-4101.
14 H. W. Zhang, L. Q. Wang, Q. F. Xiang, Q. Zhong, L. M. Chen, C. X. Xu, X. H. Xiang, B. Xu, F. Meng, Y. Q. Wan and D. Y. Deng, *Biomaterials*, 2014, **35**, 356-367.
15 S.-W. Chou, Y.-H. Shau, P.-C. Wu, Y.-S. Yang, D.-B. Shieh and C.-C. Chen, *J. Am. Chem. Soc.*, 2010, **132**, 13270-13278.
16 A. K. Duncan, P. J. Klemm, K. N. Raymond and C. C. Landry, *J. Am. Chem. Soc.*, 2012, **134**, 8046-8049.

17 C. Alric, J. Taleb, G. L. Duc, C. Mandon, C. Billotey, A. L. Meur-Herland, T. Brochard, F. Vocanson, M. Janier, P. Perriat, S. Roux and O. Tillement, *J. Am. Chem. Soc.*, 2008, **130**, 5908-5915.

18 M. Beija, Y. Li, H. T. Duong, S. Laurent, L. V. Elst, R. N. Muller, A. B. Lowe, T. P. Davis and C. Boyer, *J. Mater. Chem.*, 2012, **22**, 21382-21386.

19 D. H. Hu, Z. H. Sheng, P. F. Zhang, D. Z. Yang, S. H. Liu, P. Gong, D. Y. Gao, S. T. Fang, Y. F. Ma and L. T. Cai, *Nanoscale*, 2013, **5**, 1624-1628.

20 N. Sk Md, H.-K. Kim, J.-A. Park, Y.-M. Chang and T.-J. Kim, *Bulletin of the Korean Chemical Society*, 2010, **31**, 1177-1181.

21 A. Xia, M. Chen, Y. Gao, D. Wu, W. Feng and F. Li, *Biomaterials*, 2012, **33**, 5394-5405.

22 J. Zhou, Z. Lu, G. Shan, S. Wang and Y. Liao, *Biomaterials*, 2014, **35**, 368-377.

23 Z. Liu, F. Pu, J. Liu, L. Jiang, Q. Yuan, Z. Li, J. Ren and X. Qu, *Nanoscale*, 2013, **5**, 4252-4261.

24 J. Ryu, H.-Y. Park, K. Kim, H. Kim, J. H. Yoo, M. Kang, K. Im, R. Grailhe and R. Song, *J. Phys. Chem. C*, 2010, **114**, 21077-21082.

25 Z. Liu, F. Pu, S. Huang, Q. Yuan, J. Ren and X. Qu, *Biomaterials*, 2013, **34**, 1712-1721.

26 J. Y. Park, M. J. Baek, E. S. Choi, S. Woo, J. H. Kim, T. J. Kim, J. C. Jung, K. S. Chae, Y. Chang and G. H. Lee, *ACS Nano*, 2009, **3**, 3663-3669.

27 J. Lee, J. S. Choi and M. Yoon, *J. Mater. Chem. B*, 2014, **2**, 2311-2317.

28 V. B. Kumar, K. Kumar, A. Gedanken and P. Paik, *J. Mater. Chem. B*, 2014, **2**, 3956-3964.

29 Y. Liu, K. Ai, Q. Yuan and L. Lu, *Biomaterials*, 2011, 32, 1185-1192.

30 H. Liu, W. Lu, H. Wang, L. Rao, Z. Yi, S. Zeng and J. Hao, *Nanoscale*, 2013, **5**, 6023-6029.

31 Z. Yi, S. Zeng, W. Lu, H. Wang, L. Rao, H. Liu and J. Hao, *ACS applied materials & interfaces*, 2014, **6**, 3839-3846.

32 K. T. Yong, I. Roy, R. Hu, H. Ding, H. Cai, J. Zhu, X. Zhang, E. J. Bergey and P. N. Prasad, *Integrative biology : quantitative biosciences from nano to macro*, 2010, **2**, 121-129.

33 Y. Teow and S. Valiyaveettil, *Nanoscale*, 2010, **2**, 2607-2613.

34 D. Bhattacharya, M. Das, D. Mishra, I. Banerjee, S. K. Sahu, T. K. Maiti and P. Pramanik, *Nanoscale*, 2011, **3**, 1653-1662.

35 J. Li, X. Li, X. Sun, T. Ikegami and T. Ishigaki, *Chem. Mater*, 2008, **20**, 2274-2281.

36 I. Rehor, J. Slegerova, J. Kucka, V. Proks, V. Petrakova, M. P. Adam, F. Treussart, S. Turner, S. Bals, P. Sacha, M. Ledvina, A. M. Wen, N. F. Steinmetz and P. Cigler, *Small*, 2014, **10**, 1106-1115.

37 R. Al-Gaashani, S. Radiman, A. R. Daud, N. Tabet and Y. Al-Dourid, *Ceramics International*, 2013, **39**, 2283-2292.

38 Y. Lin, D. Wang, Q. Zhao, M. Yang and Q. Zhang, *J. Phys. Chem. B*, 2004, **108**, 3202-3206.

39 L. Jing, B. Xin, F. Yuan, L. Xue, B. Wang and H. Fu, *J. Phys. Chem. B*, 2006, **110**, 17860-17865.

40 K. K. Hammud, J. M. Mohammed, M. M. Radif, A. L. M. Raouf, S. S. Mahmmood, R. R. Neama, D. E. Znad and S. J. Abbas, *Journal of Chemical and Pharmaceutical Research*, 2013, **5**, 24-28.

41 B. Sahoo, S. P. Devi, S. K. Sahu, S. Nayak, T. K. Maiti, D. Dhara and P. Pramanik, *Biomater. Sci.*, 2013, **1**, 647-657.

42 Y. Yang, L. Ren, C. Zhang, S. Huang and T. Liu, *ACS applied materials & interfaces*, 2011, **3**, 2779-2785.

43 G. D. Venkatasubbu, S. Ramasamy, V. Ramakrishnan and J. Kumar, *Advanced Powder Technology*, 2013, **24**, 947-954.

44 Z. Li, K. Dong, S. Huang, E. Ju, Z. Liu, M. Yin, J. Ren and X. Qu, *Advanced Functional Materials*, 2014, 24, 3612-3620.

45 K. Y. Lee, E. Seow, Y. Zhang and Y. C. Lim, *Biomaterials*, 2013, **34**, 4860-4871.

46 S. A. Ansari, M. M. Khan, M. O. Ansari, J. Lee and M. H. Cho, *J. Phys. Chem. C*, 2013, **117**, 27023-27030.

47 X.-H. Ma, A. Gong, L.-C. Xiang, T.-X. Chen, Y.-X. Gao, X.-J. Liang, Z.-Y. Shen and A.-G. Wu, *J. Mater. Chem. B*, 2013, **1**, 3419-3428.

48 C. Reitz, J. Haetge, C. Suchomski and T. Brezesinski, *Chem. Mater.*, 2013, **25**, 4633-4642.

49 Y. Wu, Y. Sun, X. Zhu, Q. Liu, T. Cao, J. Peng, Y. Yang, W. Feng and F. Li, *Biomaterials,* 2014, **35**, 4699-4705.

50 Y. Dai, H. Xiao, J. Liu, Q. Yuan, P. Ma, D. Yang, C. Li, Z. Cheng, Zh. Hou, P. Yang and J. Lin, *J. Am. Chem. Soc.,* 2013, **135**, 18920-18929.

Biocompatible Folate-modified Gd^{3+}/Yb^{3+}-doped ZnO Nanoparticles for Dualmodal MRI/CT Imaging

Qi Yin,[a] Xiaoying Jin,[a,b] Guocheng Yang,[a,b] Chunhuan Jiang,[c] Zhongkai Song,[a] and Guoying Sun*[a,b]

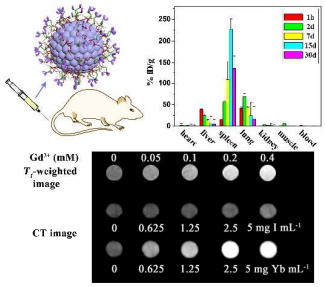

Folate-modified ZnO:Gd,Yb nanoprobes with good stability and biocompatibility can efficiently induce positive contrast enhancement in T_1-weighted MRI and CT imaging .